Chapter-5

Investigation of $(Bi_{1/2}Li_{1/2})_x Ba_{(1-x)}TiO_3$ Solid Solution for Energy Storage Applications

5.1 Introduction

Perovskite materials have shown great potential for designing materials for various applications like multilayer ceramic capacitors, energy storage and harvesting, transducers, sensors, optoelectronic devices, etc, owing to its multifunctional structure and behaviour [216-218]. In this context, the lead-free perovskite, barium titanate (BT) is most investigated base material for capacitive energy storage and photovoltaic energy harvesting applications in ceramic devices. It has unique combination of dielectric, ferroelectric and piezoelectric properties e.g. high quality factor, low dielectric loss, high polarization and good electrochemical coupling ($k_{33} \sim 50$). However, pure $BaTiO_3$ ceramics has relatively high band gap, high ferroelectric hysteresis loss, low breakdown strength and low Curie temperature (T_c) which restricts it to be fairly suitable for energy harvesting and storage applications. [219]

The squarish shaped polarization (P)-electric field (E) loop of pure $BaTiO_3$ showing very high remanent polarization (Pr) and high energy loss (W_L), is not suitable to produce large recoverable energy density (W_R). In order to achieve very high recoverable energy (W_R) and high energy storage efficiency (η) simultaneously, narrow and oblique shaped P-E loops of the material need to be obtained [108]. In this context, shape of the P-E loops of antiferroelectric materials are most suitable showing very high energy storage density but lead free antiferroelectric materials are very few and have less life cycles with stability issues [220, 221]. The second-best candidate materials are relaxor ferroelectrics which have constricted PE loops, better electro-mechanical coupling, ordering of cations, large piezoelectric coefficients and presence of chemical in-homogeneities. These properties make them to be most interesting among all ferroelectrics for capacitive energy storage applications [109, 110]. In recent decades, many lead based perovskites $Pb_{0.85}La_{0.1}(Zr_{0.65}Ti_{0.35})O_3$ (PLZT), (1-x)

$[Pb(Mg_{1/3}Nb_{2/3})O_3]$-$x[PbTiO_3]$ (PMN-PT) and $0.1Pb(Ni_{1/3}Nb_{2/3})O_3$-$0.9Pb(Zr_{0.42}Ti_{0.58})O_3$ (PNN-PZT), etc. have been explored due to relaxor ferroelectric nature with higher storage energy storage density [222, 223]. However, toxic and volatile nature of lead-based compounds restricts their large scale commercial applications.

The band Gap of BaTiO$_3$ is 3.2 eV [224] which indicates that pure BT is neither a perfect insulator nor a perfect semiconductor. Intrinsic dielectric breakdown strength of a material directly depends upon the band gap, higher the band gap, higher the strength. [225] Moreover, the materials with this range of band gap can be utilized for photovoltaic energy harvesting only in the UV range of solar spectrum. Hence, pure BaTiO$_3$ needs modification for utilization in capacitive energy storage or photovoltaic energy harvesting applications. Many attempts have been made in this direction by chemical substitution at Ba- and Ti+ sites in BaTiO$_3$, For example, Fe^{3+} doped BaTiO$_3$ [226], $Ba(Ti_{1-x}Y_x)O_{3-x/2}$ [227], $Ba_{1-x}(Bi_{0.5}Li_{0.5})_xTiO_3$ (BBLT) (x=0.3, 0.4, 0.5) [218], $Ba_{1-x}(Bi_{0.5}Li_{0.5})_xTiO_3$ $(0 \leq x \leq 0.1)$ [228] have been investigated to modulate the physical properties in such a way that it could become suitable for energy storage or harvesting applications. Substitution of different elements at either Ba/Ti site or making solid solutions with different compounds may improve the ferroelectric, optical, electrical properties, band gap, shape of P-E loop, breakdown strength and Curie temperature.

Substituting two Ba^{2+} cation by pair of Hetero-valent cation Bi^{3+} and Li^+ in BaTiO$_3$ can cause local deformation in the microstructure and can generate crystal defects which modify the electrical properties drastically [219]. This kind of substitution have tendency to disturb the long range order of ferroelectric domains and generate the nano-sized polar regions leading to relaxor behavior in the material [229]. Monovalent cation Li^+ when incorporated along with Bi^{3+} at the Ba site, maintaining charge neutrality and

stable perovskite crystal structure, relaxor behaviour is introduced for the optimum concentration [230]. Recently many Li^+ substituted $BaTiO_3$ based systems e.g. $(Bi_{1/2}Na_{1/2})TiO_3-(Bi_{1/2}K_{1/2})TiO_3-(Bi_{1/2}Li_{1/2})TiO_3-BaTiO_3$ [231], $[Bi_{1-y}(Na_{1-x-y}Li_x)]0.5Ba_yTiO_3$ [232], $Bi_{0.5}Na_{0.5}TiO_3–BaTiO_3–Bi_{0.5}Li_{0.5}TiO_3$ [233], $(Bi_{0.5}Na_{0.5})TiO_3–(Bi_{0.5}K_{0.5})TiO_3–BaTiO_3$ [234] etc. suggests that monovalent Li^+ cation is quite suitable in improving piezoelectric response, electrochemical properties, depolarization temperature and poling effects [231, 235].

The effect of Bi^{3+} and Li^+ co-substitution in $BaTiO_3$ on structural, dielectric and ferroelectric properties have been studied earlier in $Ba_{1-x}(Bi_{0.5}Li_{0.5})_xTiO_3$ ($0 \leq x \leq 0.1$) [228] and $Ba_{1-x}(Bi_{0.5}Li_{0.5})_xTiO_3$ (BBLT) (x = 0.3, 0.4 and 0.5) [218]. These two papers report contrary results like temperature dependent dielectric behavior, a little different morphology of grains and mutually opposite trend in the change of crystal structure and P-E loops with increasing co-substitution of Bi and Li. Vertical and broad P-E loops are reported in $Ba_{1-x}(Bi_{0.5}Li_{0.5})_xTiO_3$ ($0 \leq x \leq 0.1$) [14] whereas slanted P-E loops are reported with increasing concentration in $Ba_{1-x}(Bi_{0.5}Li_{0.5})_xTiO_3$ (x=0.3, 0.4 and 0.5) range. In view of this, the present work is focused to study the research gap of these two reports on $Ba_{1-x}(Bi_{0.5}Li_{0.5})_xTiO_3$ ceramics and explore the potential capacitive energy storage or photovoltaic energy harvesting applications of the developed compositions. We have investigated several compositions of $(Bi_{0.5}Li_{0.5})_xBa_{(1-x)}TiO_3$ in the range of concentrations (x=0.10, 0.12, 0.15, 0.20 and 0.25) that was not properly explored earlier. Incorporation of $(Bi_{0.5}Li_{0.5})^{2+}$ at Ba- site in this composition range may have better and interesting dielectric, ferroelectric properties, and suitable band gap for energy storage/harvesting applications.

5.2 Experimental

Traditional, low cost, solid state ceramic method was adopted to prepare $(Bi_{0.5}Li_{0.5})_x Ba_{(1-x)} TiO_3$ (x = 0.10, 0.12, 0.15, 0.20, 0.25) samples. All samples of $(Bi_{0.5}Li_{0.5})_x Ba_{(1-x)} TiO_3$ were synthesized by ball milling in a planetary grinding zirconia jars taking balls of 1 cm diameter. Analytical reagent (AR) grade $BaCO_3$ (Hi-media, 99%), $LiCO_3$ (Sigma Aldrich, 99.99%), Bi_2O_3 (Hi-media, 99%) and TiO_2 (Hi-media, 99.5%) were taken in stoichiometric ratio and ball milled in acetone medium at 200 rpm for 6 hours. Additional 2% Bi_2O_3 were taken to repay the thermal evaporation loss of Bi during high temperature calcination and sintering. Optimization of calcination temperature and time were done in open atmosphere in a muffle furnace and the optimum temperature for calcination was found to be 850°C. Then all the grinded reactant mixtures were calcined at 850°C. After mixing 2% PVA (Polyvinyl Alcohol) binder solution in water, pellets of calcined powders are formed by pressing at 6-ton uniaxial load in pelletizer. The pellets are then heated at 450°C for removal of PVA and then sintered at 900°C in the closed air condition. The capacitive energy storage device was prepared by using fast-drying silver paste electrode on both flat sides of the pellet. X ray diffraction pattern were recorded by Regaku Miniflex x-ray powder diffractometer in the 2θ range 10°-100° at the 2θ steps of 0.02°. Rietveld refinements were performed using FullProf suite software for crystal structure analysis. ZEISS EVO18 scanning electron microscope were used to take surface images for microstructural analysis. K-Alpha Thermo Fisher Scientific XPS was employed to record binding energy peaks for elemental analysis. Fitting of the XPS curves for various elements were done by XPSPEAK4.1 software. Dielectric measurements were done on electroded sintered pellet using KEYSIGHT–E4990A impedance analyzer. SHIMADZU UV-2600 UV-Vis spectrophotometer was used to record diffuse spectra in

reflectance mode for the band gap analysis. Polarization (P)-Electric field (E) hysteresis loop characterization was done by Radiant Precision Premier II ferroelectric tester using bipolar signal to determine remanent polarization (P_r) and coercive field (E_c).

5.3 Results and Discussion

5.3.1 Crystal Structure Analysis

In order to investigate the perovskite phase formation and crystal structure evolution with composition, x-ray diffraction patterns of calcined samples of $(Bi_{0.5}Li_{0.5})_x Ba_{(1-x)} TiO_3$ (x = 0.10, 0.12, 0.15, 0.20 and 0.25) were recorded at room temperature. **Fig.5.1** illustrates the XRD pattern of all five compositions in the 2θ range 10°-100°. The analysis of the XRD patterns of the compositions with x = 0.12, 0.15, 0.20 and 0.25 suggests that all these compositions crystalize into cubic phase with *Pm-3m* space group.

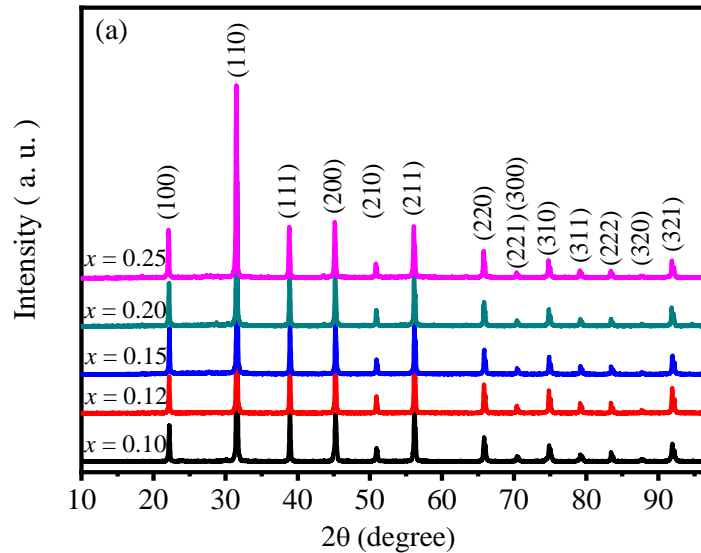**Figure 5.1:** X-ray diffraction pattern of calcined sample of $(Bi_{0.5}Li_{0.5})_x Ba_{(1-x)} TiO_3$ (x = 0.10, 0.12, 0.15, 0.20 and 0.25).

Rietveld structure refinement for all the compositions were executed using cubic crystal structure with *Pm-3m* space group and the Rietveld fits are shown in **Figs. 5.2(a-**

e). It shows good Rietveld fit along with the satisfactory refinement agreement factors as listed in **Table 1**. The table also lists the lattice parameter, unit cell volume and density of different samples.
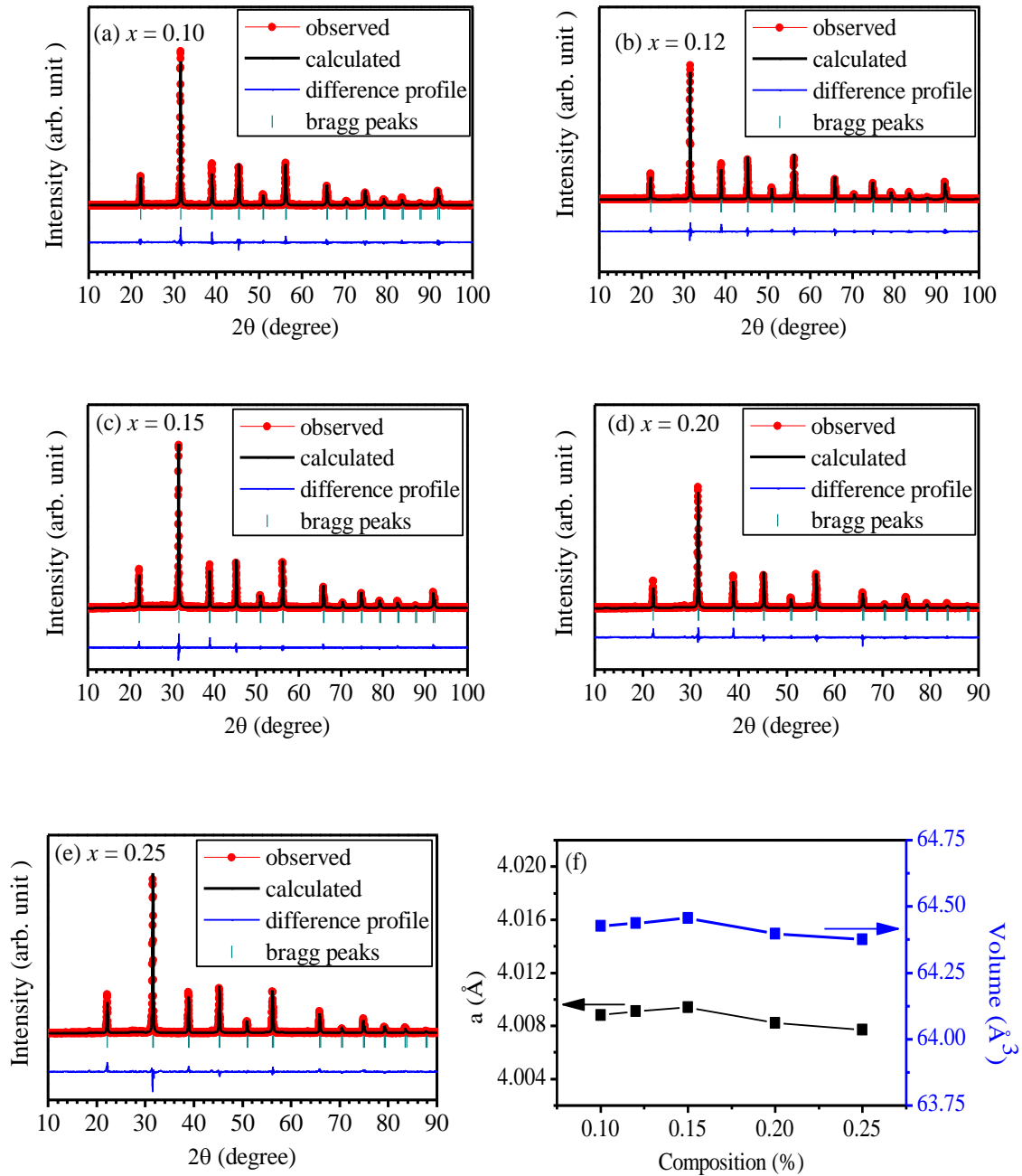

Figure 5.2: Rietveld refinement fits for X-Ray diffraction patterns of $(Bi_{0.5}Li_{0.5})_xBa_{(1-x)}TiO_3$ ceramics, (a) $x = 0.10$, (b) $x = 0.12$, (c) $x = 0.15$, (d) $x = 0.20$ and (e) $x = 0.25$. Red dots represent experimentally recorded XRD patterns, Overlapping continuous black line represent calculated patterns and bottom continuous blue curve represents the difference of the two profiles. The Bragg's peaks are represented by vertical bars. (f) Variation of lattice parameter and unit cell volume with different composition.

Table 1.1: List of refinement parameters and unit cell parameters obtained after Rietveld structure refinement for $(Bi_{0.5}Li_{0.5})_xBa_{(1-x)}TiO_3$.

Composition	$x = 0.10$	$x = 0.12$	$x = 0.15$	$x = 0.20$	$x = 0.25$
a (Å)	4.0088(7)	4.0091(1)	4.0094(7)	4.0082(3)	4.0077(9)
Volume (Å^3)	64.427(4)	64.438(3)	64.456(1)	64.396(2)	64.375(1)
R_{exp}	19.3	22.5	24.1	22.38	17.84
R_{wp}	28.3	27.6	20.7	30.14	23.8
χ^2	2.16	1.51	1.35	1.84	1.78
RF Factor	3.01	2.81	3.21	2.344	1.776
Density (g/cm^3)	5.932	5.915	5.894	5.861	5.826
Density (%)	92.14	97.05	93.67	91.54	97.25

Composition dependent variation of lattice parameters and unit cell volume is shown graphically in **Figs. 5.2(f)**. The refined unit cell parameter 'a' and volume 'V' are showing small-scale non-monotonic changes consistent with previous report for higher concentration [218, 236]. The ionic radii of both Bi^{3+} (1.17 Å) and Li^{1+} (0.92 Å) are smaller than Ba (1.42 Å). Thus, ideal substitution is expected to cause monotonic decrease in lattice parameter. However, initial small increase is observed with increasing the substituent concentration which shows some Li^+ cation very small size in comparison to Ba^{2+} may go at interstitial site. Overall decrease in lattice parameter and volume is observed for higher concentrations which is consistent with the previous report [228]. The crystal structure of the sintered samples was also obtained to be cubic as confirmed by Rietveld structure refinement. **Table 5.1** also lists the density of the sintered pellets for various compositions along with the theoretical density. The theoretical density continuously decreases with increasing composition (x).

5.3.2 SEM Analysis

Figs. 5.3(a-d) show the SEM images of the surface of the sintered ceramic pellets of $(Bi_{0.5}Li_{0.5})_x Ba_{(1-x)}TiO_3$ (x = 0.10, 0.12, 0.15 and 0.20) taken at same magnification 10 kX respectively. The surface morphology of all the samples show homogeneous and non-porous dense microstructure with spheroid shaped grains having clear grain boundaries. Archimedes principle for buoyancy effect was used to determine the density of the sintered pellets and it lies in the range of 92.5%-94% which is supposed to be good densification when sintered below 1000°C. The grain size distribution for all the compositions is shown by the histogram in **Figs. 5.3 (f-i)**. The grain size estimation from the micrographs were done with the help of image J software. The grain size distribution for all the compositions is more or less similar as shown in **5.3 (f-i)**. For all the compositions, the estimated size has variation with significant difference in minimum size and maximum size of grains showing bimodal structure. The average grain size of various samples was calculated to be 1.07μm, 1.41 μm, 1.3 μm and 1.51 μm for x = 0.10, 0.12, 0.15 and 0.20 respectively. A higher Bi-concentration is expected to help in increased densification and grain growth assisted by liquid phase sintering. It can be seen by comparing the micrographs that average grain size of $(Bi_{0.5}Li_{0.5})_x Ba_{(1-x)}TiO_3$ slightly increases with increasing substituent concentration of $(Bi_{0.5}Li_{0.5})^{2+}$ cations which is consistent with earlier reports where 30%, 40% and 50% of $(Bi_{0.5}Li_{0.5})^{2+}$ substitution were done in $BaTiO_3$ [218] but contradicts to the variation observed for low concentration (2-10%) substitution of $(Bi_{0.5}Li_{0.5})^{2+}$ in $BaTiO_3$ reported by M. Rawat et. al. [228]. Presence of larger grains can be owed to the inter-granular interaction at the contact area of grains, inducing merger of grains.
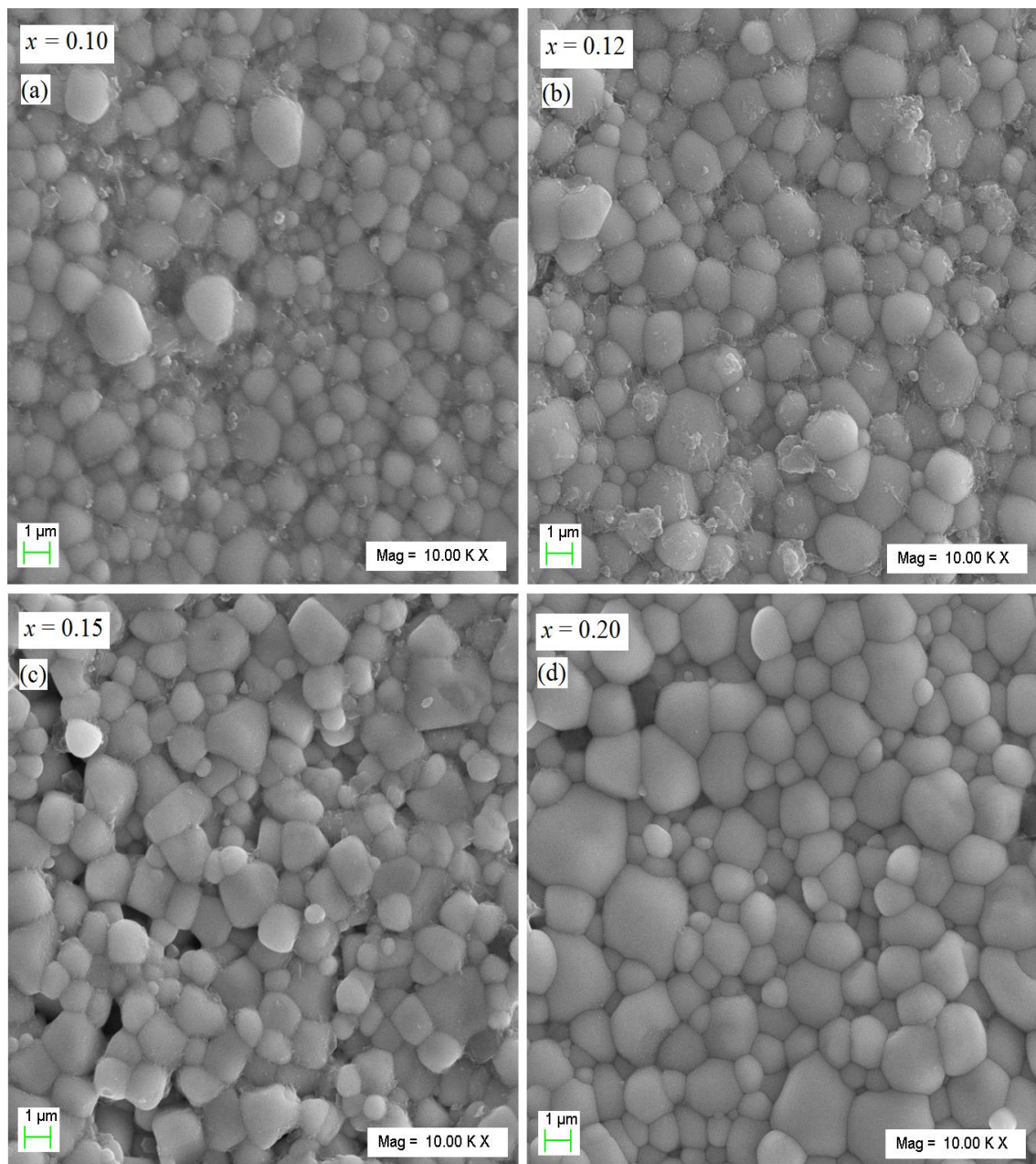
Figure 5.3: (a-d) SEM micrographs of $(Bi_{0.5}Li_{0.5})_xBa_{(1-x)}TiO_3$ (x = 0.10, 0.12, 0.15 and 0.20) pellets sintered at 950°C.
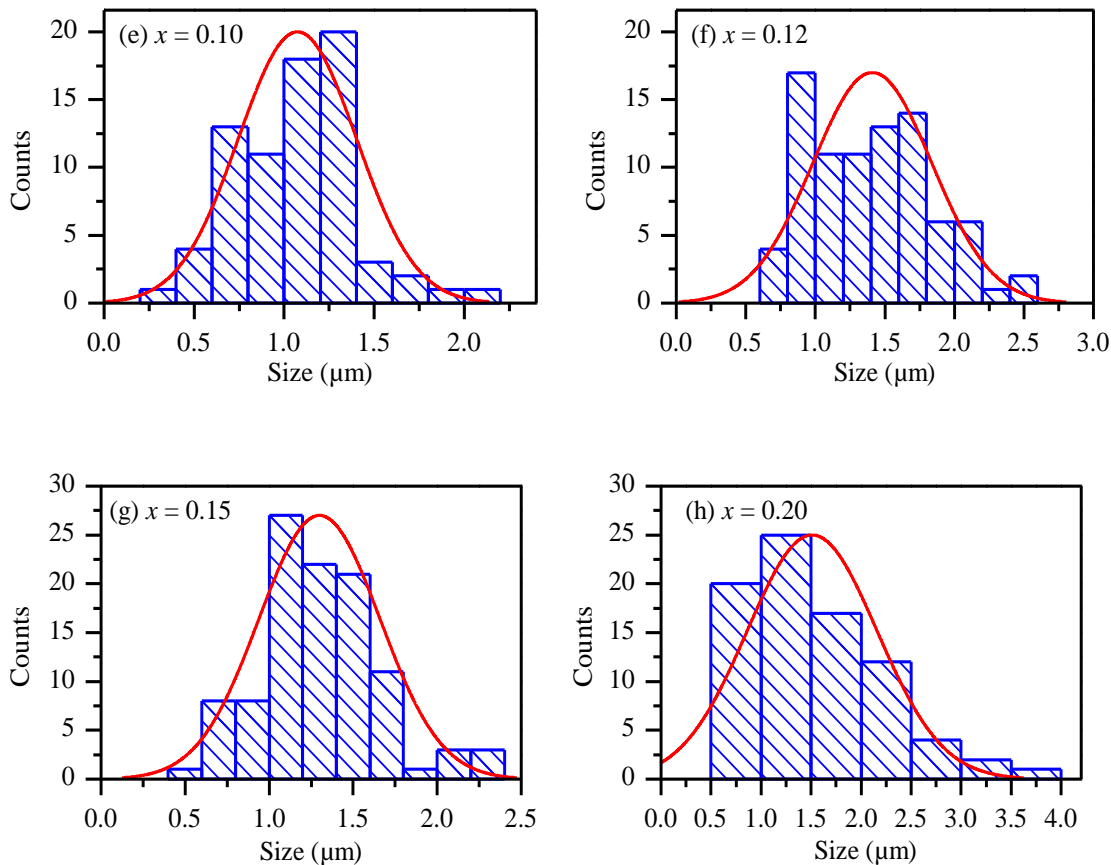
Figure 5.3: (e-h) Grain size distribution of $(Bi_{0.5}Li_{0.5})_x Ba_{(1-x)}TiO_3$ (x = 0.10, 0.12, 0.15 and 0.20) pellets sintered at 950°C.

5.3.3 XPS Analysis

Bi- and Li- both the substituent elements have tendency to oxidize in different valence states than the Ba. Therefore, it is important to identify oxidation states of the constituent ions of the prepared samples. X-ray photoelectron spectroscopy (XPS) characterization was performed to verify the oxidation states of one representative composition $(Bi_{0.5}Li_{0.5})_x Ba_{(1-x)}TiO_3$ (x = 0.12). Narrow scan spectra of Bi-4f, Li-1s, Ba-3d, Ti-2p and O-1s, is shown in the **Figs. 5.4 (a, b, c, d and e),** respectively. **Fig. 5.4(f)** shows full scan XPS survey which confirms the presence of all constituent atoms (Bi, Li, Ba, Ti and O) in the chemical composition of the sample. C1s peak located at 284.97 eV was used for calibrating binding energy (BE) peaks of different elements in the

narrow scan spectra. **Fig. 5.4(a)** reveals Bi-4f doublet peaks for $Bi^{3+}f_{5/2}$ at 164.17 eV and $Bi^{3+}f_{7/2}$ at 158.87 eV with single peak fits, confirming the presence of Bi element in the +3-oxidation state. Analysis of peak position and the spin orbit splitting energy (5.3 eV) of Bi-4f state on the basis of literature reports, supports Bi to be in +3 oxidation state [190, 191]. In **Fig. 5.4(b)**, the BE peak of Li is observed to be broad and weakly centered at 55.32 eV, which is expected for Li being very light atom and BE peak at 55.32 eV corresponds to +1 oxidation state of Li. As can be seen in **Fig. 5.4(c)**, two XPS peaks of Ba-3d are identified as Ba^{2+} $3d_{3/2}$ at 793.87 eV and Ba^{2+} $3d_{5/2}$ at 778.55 eV, with splitting energy separation of 15.32 eV confirming +2 oxidation state. The binding energy peaks for Ti-2p, located at 457.81 eV and at 464.61 eV, confirm doublet BE peak related to +4 oxidation states, corresponding to Ti^{4+} $2p_{3/2}$ and Ti^{4+} $2p_{1/2}$ respectively. **Fig. 5.4(e)** shows the deconvolution of Oxygen 1s BE energy peak, into two peaks at 529.71 eV and 531.88 eV. The first peak located at lower energy corresponds to lattice oxygen (O_I) and the other peak situated at high energy, relates to the oxygen deficient regions (O_{II}). Comparison of area under the curve of these two peaks (O_I : O_{II}) are estimated to be 77:23, showing presence of 23% oxygen deficient vacancies. Such a large vacancy is expected due to hetero-valent (Li^{1+}/Bi^{3+}) substitution at A (Ba^{2+}) site in $BaTiO_3$.
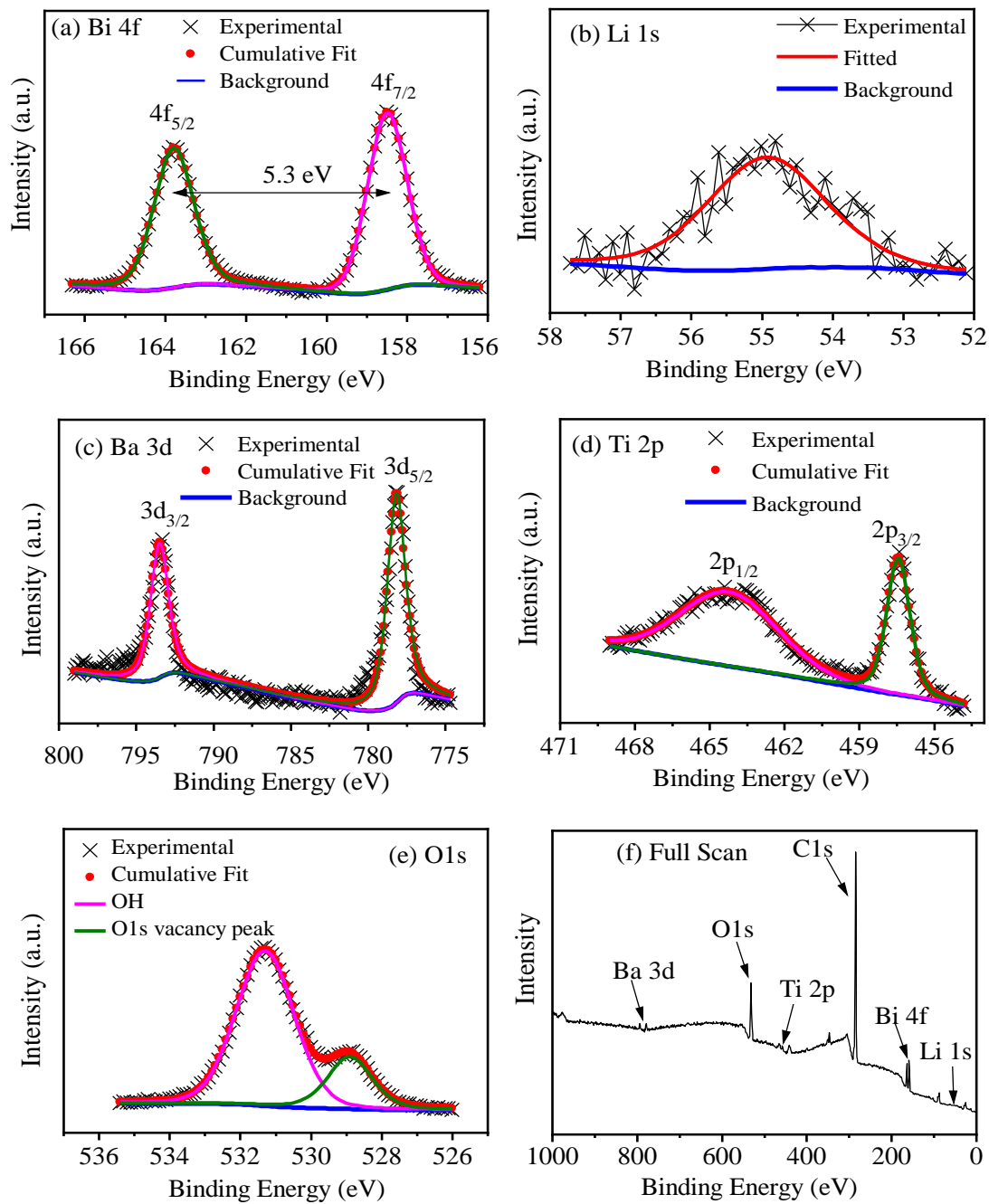
Figure 5.4: XPS spectrum of (a) Bi-4f (b) Li-1s (c) Ba-3d (d) Ti-2p (e) O-1s and (f) Full scan elemental survey for $(Bi_{0.5}Li_{0.5})_xBa_{(1-x)}TiO_3$ (x = 0.12) (Observed data is represented by black cross or black cross with black connecting lines, cumulative fitted curve is represented by overlapping red sphere or red solid line, background is represented by solid blue line and identification peaks are represented by magenta and olive solid lines).

138

5.3.4 Dielectric Analysis

Temperature dependent permittivity of $(Bi_{0.5}Li_{0.5})_xBa_{(1-x)}TiO_3$ (x = 0.10, 0.12, 0.15, 0.20 and 0.25), were recorded from 40°C to 500°C in the frequency range 20Hz-1MHz. Thermal heating were done through a programmable furnace at the rate of 2°C/min and the measurement were taken in the heating run by parallel plate capacitance method. **Figs. 5.5(a-e)** demonstrate the variation of real permittivity with temperature for compositions with x = 0.10, 0.12, 0.15, 0.20 and 0.25 respectively. As shown in **Fig. 5.5 (a)** two broad diffuse peaks are observed in the temperature variation of permitivity for the composition with x = 0.10. The first peak observed around 190°C for x=0.10 has been correlated to the transition of the coexisting local tetragonal phase to cubic phase previously in literature [228]. However, since the permitivity peaks almost diminish for higher frequencies, it can be clearly concluded that they are originating from the defect dipole relaxation-based mechanism due to different charge states of $Ba^{2+}/Li^{1+}/Bi^{3+}$ ions at A-site of the perovskite structure. As can be seen from the **Figs. 5.5(b-e)** the first relaxational peak weakens significantly and disappears with increasing compositions. The permitivity peak with temperature variation also shifts to the higher temperature side for compositions x = 0.12, 0.15, 0.20 and 0.25. The frequency dependent diffused peak observed around 500°C in all the compositions may be due to dielectric relaxation of the defect charge nano polar regions. The dielectric permitivity at 100°C for all different compositions measured in the frequency range 20Hz to 1 MHz is shown in **Fig. 5.5(f)**. It can be noticed that exceptionally high permittivity values are observed for composition with x = 0.12 across all frequency range whereas lowest permittivity values are observed for composition with x = 0.25. This result is further emphasized by **Fig. 5.5(g)** where permittivity of different

compositions is shown from room temperature (40°C) to 200°C at 1 kHz frequency. The rapid increase in dielectric permitivity and frequency dispersion at the high temperature can be explained due to enhanced of thermally activated charge carriers.
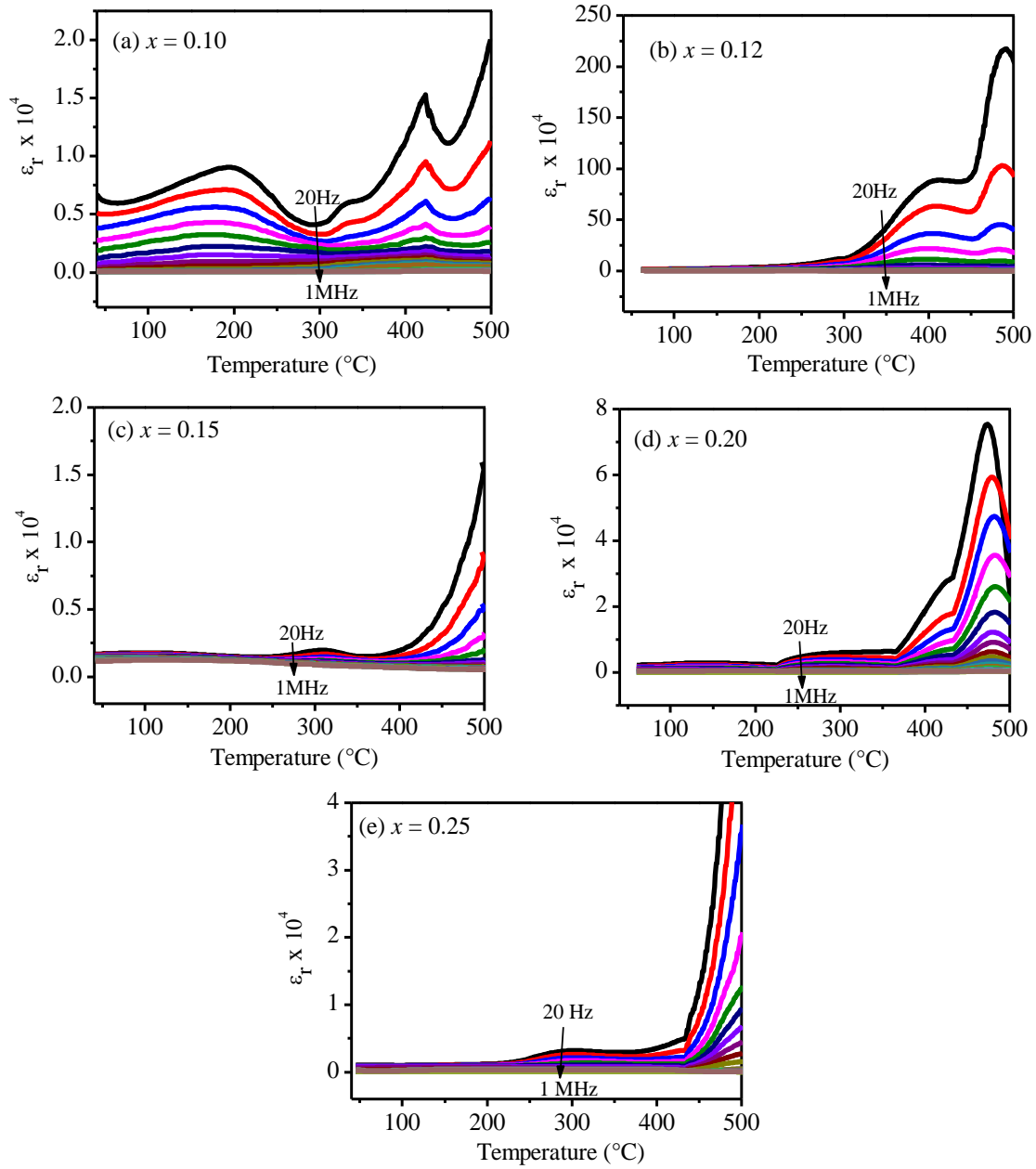

Figure 5.5: (a-e) Relative permittivity variation with temperature at various frequencies for different compositions of $(Bi_{0.5}Li_{0.5})_xBa_{(1-x)}TiO_3$ (x = 0.10, 0.12, 0.15 , 0.20 and 0.25)
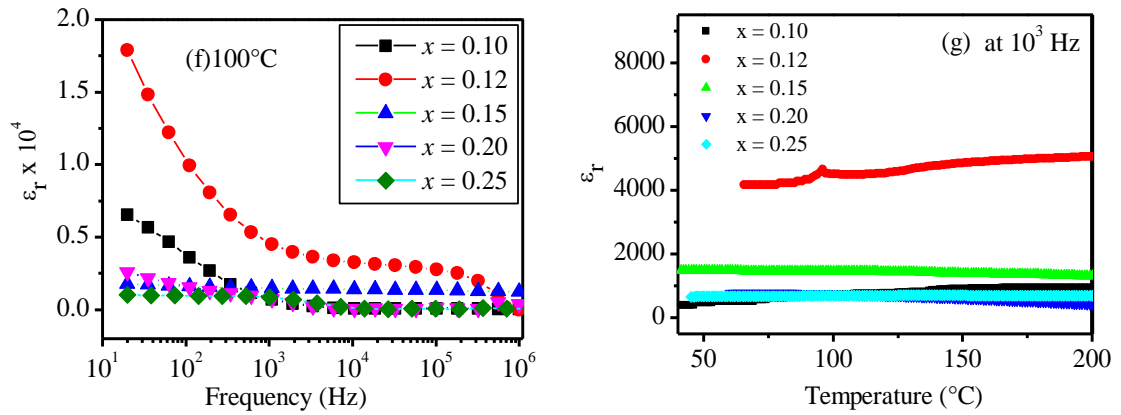
Figure 5.5: (f) Frequency variation of dielectric constant at 100°C (g) Temperature variation of permittivity for different compositions at 10^3 Hz of $(Bi_{0.5}Li_{0.5})_xBa_{(1-x)}TiO_3$ (x = 0.10, 0.12, 0.15 , 0.20 and 0.25).

5.3.5 Complex Impedance Study

Impedance spectroscopy were done to analyze the electrical transport behavior of polycrystalline sintered samples of $(Bi_{0.5}Li_{0.5})_xBa_{(1-x)}TiO_3$ (x = 0.10, 0.12, 0.15 , 0.20 and 0.25) over 20Hz to 1MHz frequency and 40°C to 500°C temperature range. Sintered polycrystalline oxide ceramics may exhibit semiconducting grains, surrounded by less conducting grain boundaries primarily due to presence of higher oxygen vacancies in interior region than the grain boundaries [150, 151]. This is because of the fact that oxygen vacancies formed at high sintering temperature are partially compensated at the grain boundaries while cooling to the room temperature. Nyquist plot between reactive component of impedance (Z'') and resistive component of impedance (Z') is used to estimate the total impedance as well as the contribution of the bulk (grain) and grain boundary resistances [151-153]. Nyquist plots of $Bi_{0.5}Li_{0.5})_xBa_{(1-x)}TiO_3$ at temperature 500°C are shown in **Figs. 5.6(a-e)** for different compositions x = 0.10, 0.12, 0.15 , 0.20 and 0.25 respectively. Plots for all the compositions are nearly semicircular with its centers depressed below the Z' (real) axis. The arcs of semicircular curves corresponding to high frequency region appear to pass through the origin

141

whereas low frequency arcs make positive intercepts at real axis for all the compositions. Whenever the grain boundary resistance contribution to total resistance is much higher than grain resistance contribution, a single semicircular arc is obtained.
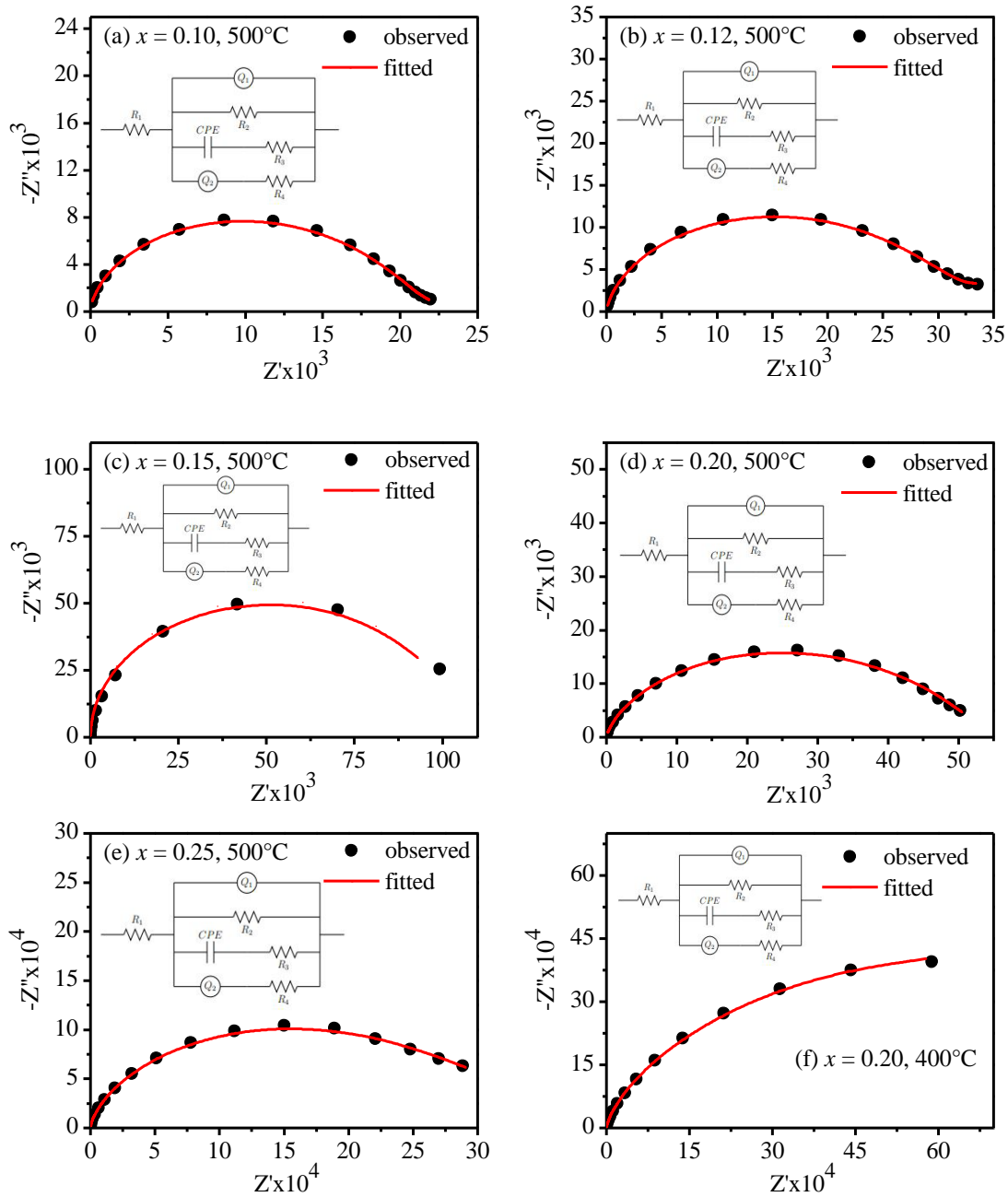

Figure 5.6: Fitted Nyquist plots for $(Bi_{0.5}Li_{0.5})_xBa_{(1-x)}TiO_3$ (x = 0.10, 0.12, 0.15 , 0.20 and 0.25) measured at 500°C (a) x = 0.10 (b) x = 0.12 (c) x = 0.15 (d) x = 0.20 (e) x = 0.25 and (f) x = 0.20 at 400°C.
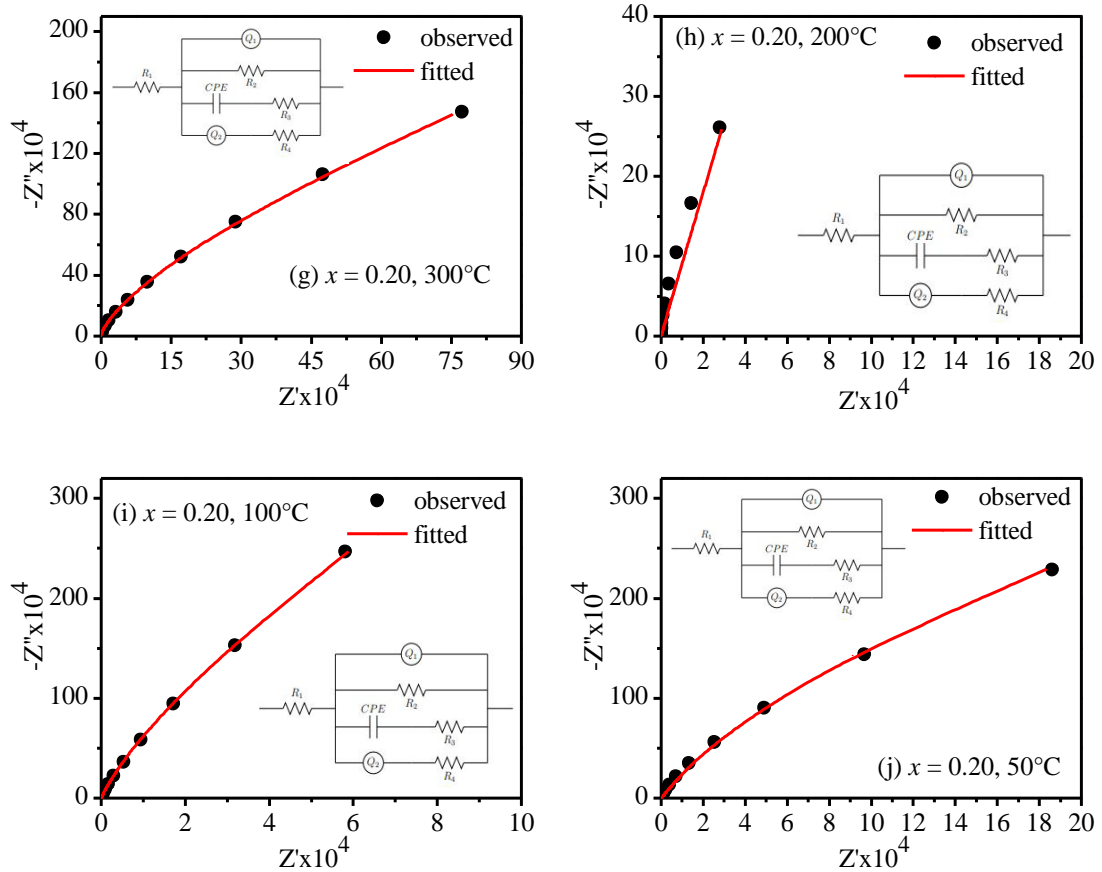
Figure 5.6: (g-j) Fitted Nyquist plots at different temperatures 400°C, 300°C, 200°C,100°C and 50°C for $(Bi_{0.5}Li_{0.5})_x Ba_{(1-x)}TiO_3$ with $x = 0.20$.

Such a scenario is observed in **Figs. 5.6** for all the samples, the resistance of grain boundaries is dominating over the resistance of grains or electrodes, resulting into a single semicircular [197, 198]. The intercept of semicircular arc on real axis on the low frequency side, determines the total resistance i.e., the resistance of grains and grain boundaries.

Nyquist plot is characterized by an equivalent electrical circuit having the equivalent contribution of impedances. The plot is best fitted by an equivalent circuit with at least a resistance and capacitance as parallel RC circuit, for each semicircular curve. Nyquist plot fitting were done by ZSIMP-WIN version-2 software and corresponding compound resistances were estimated. DC conductivity (σ) of these samples can be estimated

using formula $\sigma = \dfrac{L}{SR}$; where S is the area of the surface of the pellet, L the thickness

of pellet and R is the resistance of the grains [156]. The total resistance and hence the

conductivity calculated from above formula for various compositions of $(Bi_{0.5}Li_{0.5})_x Ba_{(1-x)}TiO_3$ (x = 0.10, 0.12, 0.15 , 0.20 and 0.25) are listed in **Table 5.2**. It can be concluded

from **Table 5.2** that; conductivity has overall decreasing trend with increasing Bi-Li

substituent concentration making it favourable for measurement of ferroelectric

properties. **Table 5.3** lists the temperature dependent conductivity of the compositions

$(Bi_{0.5}Li_{0.5})_x Ba_{(1-x)}TiO_3$ (x = 0.20) at 50°C, 100°C, 200°C, 300°C, 400°C and 500°C. The

conductivity is increasing at higher temperatures showing the semiconductor behaviour

of the material.

Table 5.2: DC impedance and conductivity of $(Bi_{0.5}Li_{0.5})_x Ba_{(1-x)}TiO_3$ (x = 0.10, 0.12, 0.15 , 0.20 and 0.25).

Composition	Compound Resistance $R_g + R_{gb}$ (Ω)	DC Conductivity σ (S/m)
x = 0.10	2.2×10^4	7.35×10^{-4}
x = 0.12	3.3×10^4	4.66×10^{-4}
x = 0.15	1.1×10^5	1.39×10^{-4}
x = 0.20	5.5×10^4	2.71×10^{-4}
x = 0.25	3.4×10^5	7.52×10^{-5}

Table 5.3. DC impedance and DC conductivity of $(Bi_{0.5}Li_{0.5})_x Ba_{(1-x)}TiO_3$ (x = 0.20) at various temperatures.

Composition	Temperature (°C)	Compound Resistance $R_g + R_{gb}$ (Ω)	DC Conductivity σ (S/m)
x = 0.20	500	5.5×10^4	2.71×10^{-4}
	400	1.4×10^6	1.07×10^{-5}
	300	8.1×10^7	1.84×10^{-7}
	200	9.9×10^7	1.51×10^{-7}
	100	5.3×10^7	2.81×10^{-7}
	50	5.4×10^7	2.76×10^{-7}

5.3.6 Band Gap Analysis:

The band gap energy for semiconductors is obtained by Tauc plot described by the Kubelka-Munk function against photon energy $h\nu$ in the UV-vis spectroscopic characterization. The mathematical relationship can be given by $(\alpha h\nu)^2 = A(h\nu - E_g)$; where 'n' is the electronic transition constant, n = ½ for allowed indirect band gap semiconductor, n = 2 for allowed direct band gap [127]. A, α, $h\nu$ and E_g are band tailoring constant, absorption coefficient, photon energy and band gap of the semiconductor respectively.

Fig. 5.7 shows the Tauc plots for different compositions of $(Bi_{0.5}Li_{0.5})_x Ba_{(1-x)}TiO_3$ (x = 0.10, 0.12, 0.15, 0.20 and 0.25) ceramics. The band gap energies were determined by extrapolating linear part of the plot to energy axis and were found to be 3.15 eV, 3.09 eV, 3.27 eV, 3.25 eV and 3.27 eV for x = 0.10, 0.12, 0.15, 0.20 and 0.25, respectively. It can be seen that all compositions have band gap above 3 eV, lying in the UV region. The minimum band gap (3.09 eV) is observed for x = 0.12 and maximum about~ 3.27 eV for x = 0.25. Thus co-substitution of Bi and Li, to some concentration decreases the band gap to some extent, but further substitution shows increment in the band gap. Overall Bi-Li doping at A site in $BaTiO_3$ does not reduce the band gap that much as reported for the B-site doping [22]. As the valence band maximum consists of primarily oxygen 2p-orbitals, and conduction band minimum consists of 3d-orbitals of B-site transition metal cation, the B-site substitution has more impact on the band gap. In $(Bi_{0.5}Li_{0.5})_x Ba_{(1-x)}TiO_3$ system, only A-site is substituted which is not involved directly in the formation of the band gap [19, 237, 238].

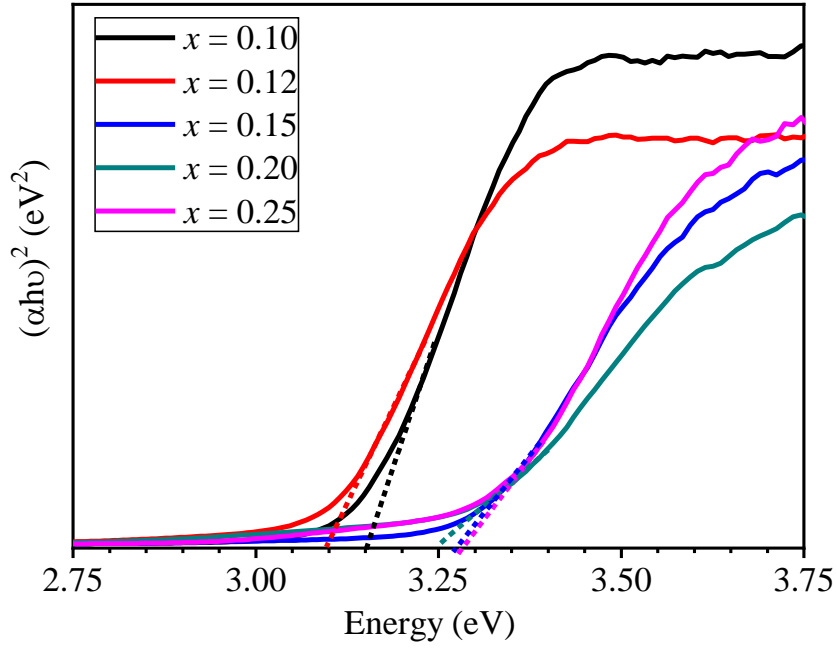**Figure 5.7:** Tauc plots with extrapolated band gap for $(Bi_{0.5}Li_{0.5})_x Ba_{(1-x)}TiO_3$ ($x = 0.10, 0.12, 0.15, 0.20$ and 0.25) ceramics.

5.3.7 Ferroelectric Characterization:

The substitution effect of $(Bi_{0.5}Li_{0.5})^{2+}$ at Ba-site in $BaTiO_3$ on ferroelectric properties, was characterized by hysteresis loop measurements at various fields and frequencies. Hysteresis plots (P-E loop) for all the compositions of $(Bi_{0.5}Li_{0.5})_x Ba_{(1-x)}TiO_3$ ($x = 0.10, 0.12, 0.15, 0.20$ and 0.25), recorded at room temperature and at 10Hz are shown individually in **Fig. 5.8 (a-e)**. Further, **Figure 5.8(f)** shows the loops of different compositions collectively, taken at same applied electric field (40 kV) for vivid comparison of the shape of the loops. **Figure 5.8(g-h)** illustrates P-E loops variation measured at different frequencies of applied voltage signal for x = 0.15 and x= 0.25 respectively. The thickness of the samples, taken for P-E loop tracing were in the 1mm-1.2mm, range and the electric signal was applied at constant frequency of 10 Hz.
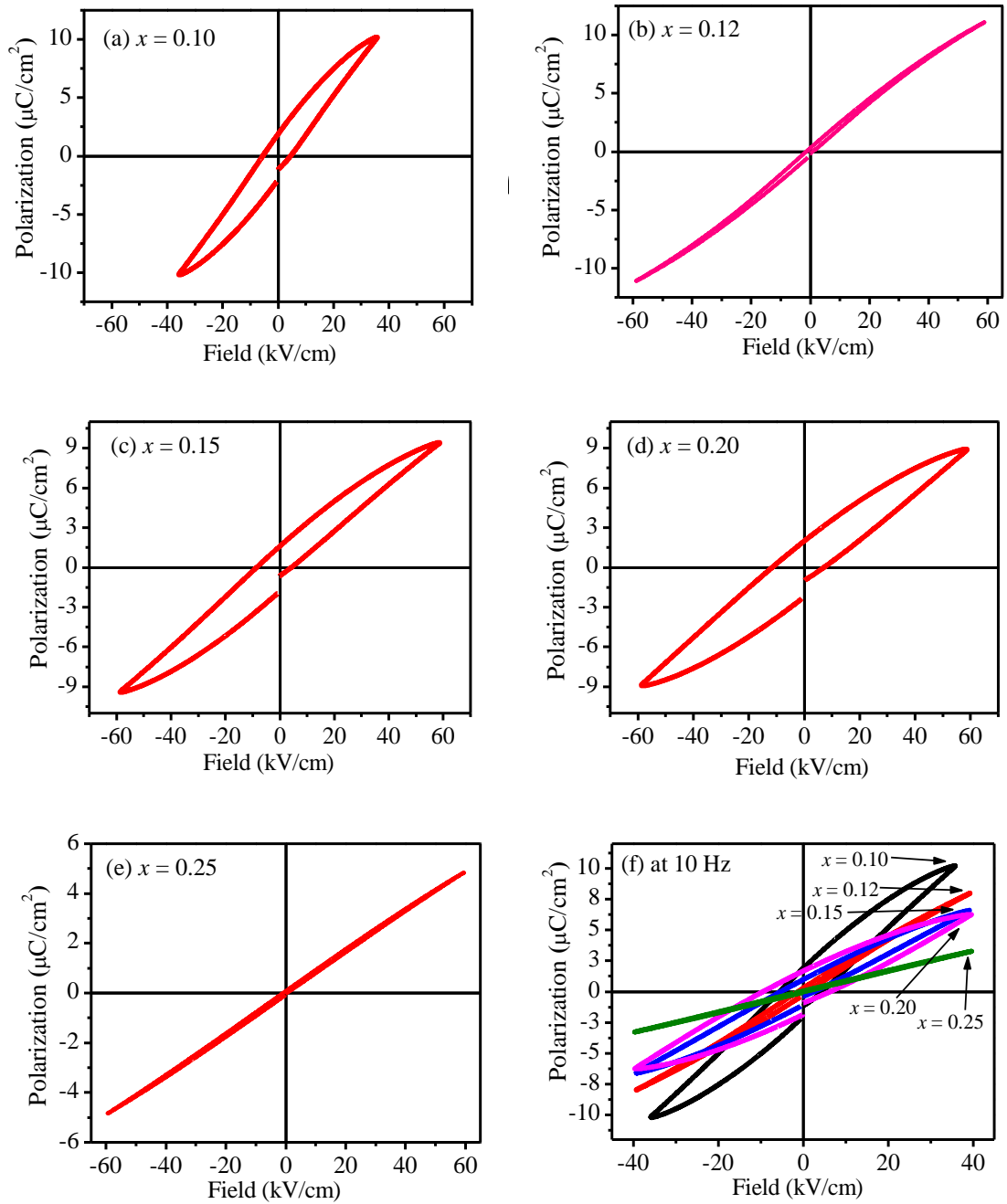
146

Figure 5.8: Room temperature P-E loops measured at 10Hz for $(Bi_{0.5}Li_{0.5})_xBa_{(1-x)}TiO_3$

(a) $x = 0.10$, (b) $x = 0.12$, (c) $x = 0.15$, (d) $x = 0.20$, (e) $x = 0.25$; (f) combined P-E loops of $(Bi_{0.5}Li_{0.5})_xBa_{(1-x)}TiO_3$ ($x = 0.10$, 0.12, 0.15, 0.20 and 0.25) compositions recorded at 10Hz

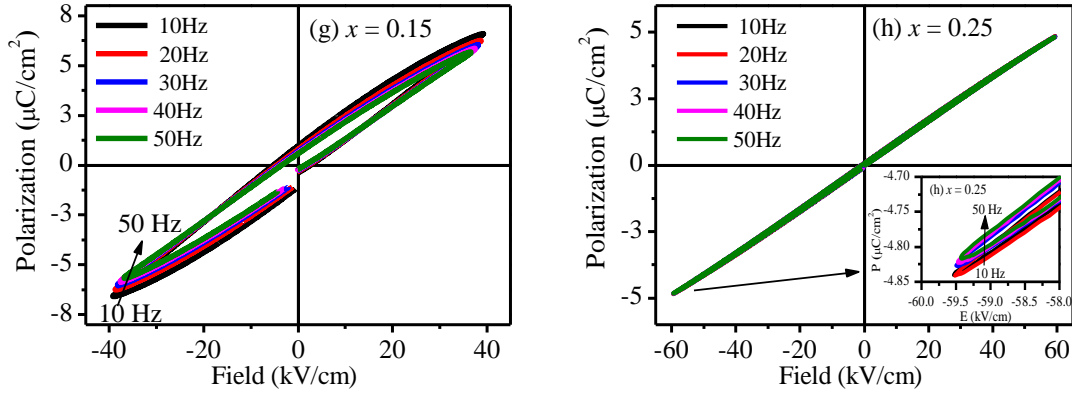**Figure 5.8:** Room temperature P-E loops measured at different frequencies for $(Bi_{0.5}Li_{0.5})_x Ba_{(1-x)}TiO_3$ (g) $x = 0.15$ and (h) $x = 0.25$.

It can be noted that shape of the P-E loops varies with the variation of the $(Bi_{0.5}Li_{0.5})^{2+}$ concentration. Slim and unsaturated P-E loops were observed for all the compositions showing signature of relaxor behaviour. Extremely thin and slanted P-E loops are obtained for two compositions, x = 0.12 and 0.25, indicating their potential suitability for capacitive energy storage application. Energy storage of a dielectric material is estimated by the area enclosed under the charge/discharge curve and polarization axis calculated with the help of the following formulae:

$$Total\ Energy\ Storage\ density\ (W_C) = \int_0^{P_{max}} E dP$$

$$Recoverable\ Energy\ Storage\ density\ (W_R) = \int_{P_r}^{P_{max}} E dP$$

$$Efficiency\ (\eta) = \frac{W_R}{W_C} \times 100\%$$

Where P is the polarization and P_r is the remanent polarization, E is the Electric field applied and P_{max} is the maximum polarization [239]. Total energy storage density (W_C), recoverable energy density (W_R) and energy loss density (W_L) have been estimated for all the compositions for maximum applied field of 60 kv/cm, and is listed in **Table 5.4**.

148

It can be seen that energy storage density at 60 kv/cm applied field is obtained highest (W_C = 308.58 mJ/cm^3) for x = 0.12, among all the different compositions with energy storage efficiency η = 94.5% . Whereas efficiency was observed highest (η = 96%) for x = 0.25 with W_C = 143 mJ/cm^3. Applied field E_{max} was further increased for x = 0.12 composition up to 80 kv/cm and hysteresis loop corresponding to 70 kv/cm and 80 kv/cm along with the storage calculation are shown in **Fig. 5.9**. Further increase in the applied field led to breakdown of the material. At highest sustainable electric field (80 kV/cm), it shows the increased storage density than storage density at 70 kV/cm but with the drop in efficiency. In **Table 5.5**, these results are compared with the BaTiO$_3$ based other dielectric materials, reported in literature. It can be observed from **Table 5.5,** that storage efficiency estimated in this work although with lower energy density, is far better than the previously reported results, suitable for multiple cycle use in thermally sensitive devices. The recoverable storage density (W_R) can also be improved further, in the thin film form of this material where obtained breakdown strength can be relatively very high. Thin film form of this material has high potential to achieve the high 'W_R' and high 'η' simultaneously for large scale industrial applications in capacitive energy storage devices.

Table 5.4. Comparison of energy storage density and Energy storage efficiency for different compositions of $(Bi_{0.5}Li_{0.5})_x Ba_{(1-x)}TiO_3$ at maximum applied field of 60 kV/cm.

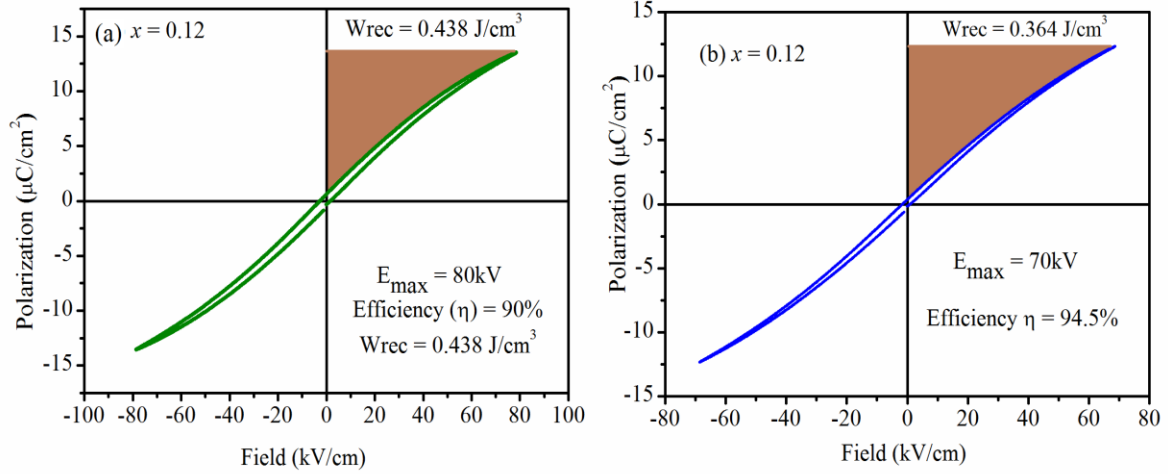| Composition	Total energy storage density W_C (mJ/cm^3)	Recoverable energy density W_R (mJ/cm^3)	Loss of energy density W_L (mJ/cm^3)	Energy storage Efficiency η (%)
x = 0.10	204.8	129.1	75.7	63.0
x = 0.12	308.58	291.7	16.88	94.5
x = 0.15	295.23	197.48	97.75	66.9
x = 0.20	300.3	173.88	126.42	57.9
x = 0.25	143.25	137.46	5.79	96.0

Figure 5.9: P-E hysteresis loops showing the stored energy density and energy loss density for $(Bi_{1/2}Li_{1/2})_{0.12}Ba_{0.88}TiO_3$ ceramics at (a) 80kV and (b) 70kV.

Table 5.5: A comparison of W_C and η from different earlier reports and the present work.

Material Name	W_C (J cm^{-3})	E (kV cm^{-1})	η (%)	Ref. No.
0.90BNTBT-0.10NaNbO$_3$	0.70	70	0.64	[240]
0.96BNTBKT-0.04BaZrO$_3$	0.73	70	0.75	[241]
0.94BNTBT-0.06KNbO$_3$	0.89	100	0.73	[242]
0.084BiTi$_{0.5}$Zn$_{0.5}$O$_3$-0.916(0.935Bi$_{0.5}$Na$_{0.5}$TiO$_3$-0.065BaTiO$_3$)	1.04	95	0.59	[243]
0.85(BF-BT)-0.15BZN	0.25	80	0.91	[244]
BL0.12B0.88T	**0.30**	**60**	**0.945**	**This work**
BL0.12B0.88T	**0.44**	**80**	**0.90**	**This work**
BL0.25B0.75T	**0.14**	**60**	**0.96**	**This work**

The P_r, E_c, and P_{max} values for various compositions of Bi and Li co-doped BaTiO$_3$ show a significant drop, which suggests that this factor has a significant influence on the polarization response, indicating the evolution process from normal ferroelectric to relaxor ferroelectric [245]. Doping of multiple charge elements induces ordering of

cations and formation of nano polar regions. The applied electric field does not induce a long-range ferroelectric phase; rather, it just aligns the polar nano regions (PNRs) [33]. As a result, the hysteresis loops for P and E become inclined and slim remarkably. After the electric field being removed, the PNRs can revert to their initial state, and all of the dipoles that have been stored can be discharged [245, 246]. Hysteresis loops for all the different compositions are much slimmer than hysteresis loop of pure $BaTiO_3$ which shows relatively low hysteresis loss as well as low dielectric loss [245-247].

5.4 Conclusions

Polycrystalline lead free fine powder of $(Bi_{0.5}Li_{0.5})_xBa_{(1-x)}TiO_3$ (x = 0.10, 0.12, 0.15 , 0.20 and 0.25) were prepared successfully by solid state method. Morphological, structural, optical, dielectric, electrical and ferroelectric properties have been studied in detail. X-ray diffraction studies reveal that all the compositions can be characterized with single phase cubic crystal structure and lattice constant does not show much change with rise in $(Bi_{0.5}Li_{0.5})^{2+}$ concentration. Average size of grains was observed to become larger with increased $(Bi_{0.5}Li_{0.5})^{2+}$ substitution effect. Improved and thermally stable dielectric properties are observed where permittivity for composition with x = 0.12 is found to be exceptionally high among all doped compositions. Nyquist plots for all compositions show a single semicircular curve, which reduces significantly with rise in temperature, showing behavior similar to semiconducting behavior. The DC conductivity estimated from these plots is observed to be decreasing with increasing substituent concentration. Band gap is found to be slightly reduced for x = 0.12 substitution and then increases gradually for higher concentration (x > 0.12). The two compositions with x = 0.12 and 0.25 were observed to have extraordinary storage efficiency of ~95% and 96% with good energy storage density useful to mitigate the heat dissipation problems in thermally sensitive charge storage devices. Conclusively,

novel composition of $(Bi_{0.5}Li_{0.5})_xBa_{(1-x)}TiO_3$ with $x = 0.12$, which have low sintering temperature, high efficiency~ 95% with good energy storage density and band gap around 3 eV seems to be promising material for energy storage applications.